Continuous-Control-Set Model Predictive Control-Based Energy Routing With Over/Under Voltage Protection

Haojun Qin, *Student Member, IEEE*, Chang Liu, *Student Member, IEEE*, Yang Shi, *Fellow, IEEE*, Ming Liu, *Senior Member, IEEE*, and Chengbin Ma, *Fellow, IEEE*

***Abstract*—Multiactive-bridge (MAB) converters are highly promising as energy routers in renewable energy applications. Their multiple-input multiple-output control challenges can be effectively addressed by a model predictive control (MPC) approach, which minimizes the interference between different ports and simplifies the controller design. However, during the optimization process, the input and output constraints are usually ignored to simplify the implementation, which may degrade the control performance and lead to large voltage overshoot/undershoot when the constraints are violated. Meanwhile, solving the constrained MPC problem within a short sampling time poses a huge computational challenge. To address these issues, in this article a continuous-control-set model predictive control (CCS-MPC) scheme is developed for the MAB converters, which incorporates input and output constraints to achieve over/under voltage protection. An MPC problem with multiple constraints is formulated and converted into a quadratic programming (QP) problem. Its real-time implementation on a low-cost microcontroller unit is further discussed including QP solver deployment, real-time certification, and delay compensation. Finally, the developed CCS-MPC scheme is experimentally verified by a four-port 500 W energy router prototype and well demonstrates the over/under voltage protection capability.**

***Index Terms*—Continuous-control-set model predictive control (CCS-MPC), multiactive-bridge (MAB) converter, over/under voltage protection (OVP/UVP), quadratic programming (QP).**

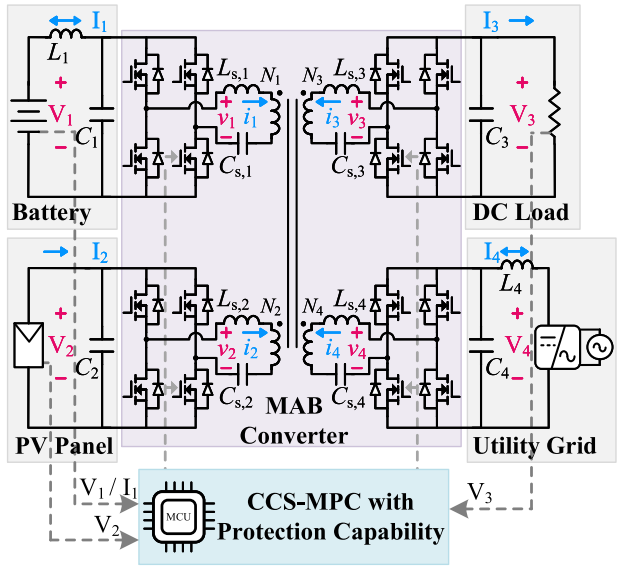

Fig. 1. Example configuration of an MAB converter under CCS-MPC controller with protection capability.

I. Introduction

MULTIACTIVE bridge (MAB) converters have attracted much attention in recent decades due to their advantages, such as galvanic isolation, bidirectional power flow, reduced number of magnetic components, and high integration and power density. They have a potential to become energy routers in dc microgrids, battery storage systems, photovoltaic (PV) power plants, and many other multiport power conversion applications [1]. Fig. 1 shows the configuration of an example four-port MAB converter that enables energy routing between battery, PV panel, dc load, and utility grid. A multiwinding transformer interconnects various energy sources and loads through multiple H-bridges and their auxiliary networks. This configuration improves system efficiency, integration, and power density. However, the single transformer also introduces cross-coupling of power flows and complicates the control of the MAB converters, which is essentially a multiple-input multiple-output (MIMO) control problem.

The most popular approach currently is to decompose the original MIMO control system into several independent single-input single-output (SISO) control loops and combine a decoupling solution to mitigate the cross-coupling effect. Existing decoupling solutions can be roughly divided into two categories: hardware-based and algorithm-based ones. A straightforward hardware-based solution is to remove the series inductance (e.g., $L_{s,i}$ in Fig. 1) at a specific port such that the voltage and flux variations are clamped and the cross-coupling can be inherently eliminated [2], [3], [4]. A winding arrangement method has been

Received 27 May 2025; revised 18 August 2025; accepted 4 October 2025. Date of publication 15 October 2025; date of current version 19 January 2026. This work was supported by the National Natural Science Foundation of China under Grant 52077132. Recommended for publication by Associate Editor Q. Shafiee. *(Corresponding author: Chengbin Ma.)*

Haojun Qin, Chang Liu, and Chengbin Ma are with the University of Michigan-Shanghai Jiao Tong University Joint Institute, Shanghai Jiao Tong University, Shanghai 200240, China (e-mail: haojun.qin@sjtu.edu.cn; shangyuliuchang@sjtu.edu.cn; chbma@sjtu.edu.cn).

Yang Shi is with the Department of Mechanical Engineering, University of Victoria, Victoria BC V8W 2Y2, Canada (e-mail: yshi@uvic.ca).

Ming Liu is with the School of Electronic Information and Electrical Engineering, Shanghai Jiao Tong University, Shanghai 200240, China (e-mail: mingliu@sjtu.edu.cn).

Color versions of one or more figures in this article are available at https://doi.org/10.1109/TPEL.2025.3622080.

Digital Object Identifier 10.1109/TPEL.2025.3622080

TABLE I
COMPARISON OF RECENT QP SOLVER-BASED CCS-MPC SCHEMES IN POWER ELECTRONICS APPLICATIONS

Ref.	Application	QP solver	Control Platform	Sampling Time	Horizon Length	Output Constraints
[18]	Load-commutated inverter-fed synchronous machines	qpOASES	AC 800PEC (ABB's industrial controller)	1 ms	10	No
[19]	Induction motor drives	qpOASES	dSPACE MicroLabBox	100 μs	2	No
[20]	Synchronous motor drives	qpOASES	dSPACE MicroLabBox	100 μs	3	No
[21]	Reluctance synchronous machines	qpOASES	dSPACE MicroLabBox	250 μs	2	No
[22]	Medium-voltage drives	Sphere decoding	dSPACE DS1106	125 μs	1–4	No
[23, 24]	Voltage forming grid inverters	–	dSPACE SCALEXIO	100 μs	2	Yes
[25]	Permanent magnet Synchronous machines	Primal-dual interior-point	dSPACE DS1007	125 & 100 μs	2	Yes
[26]	Neutral point clamped converters	qpOASES	Zynq UltraScale+MPSoC (2 ARM + 1 FPGA)	666 μs	4	Yes
This work	MAB converters	OSQP	STM32H723VGT6 (Cortex-M7 ARM)	200 μs	3	Yes

proposed to minimize the leakage inductance of a multiwinding transformer [5]. However, these hardware-based decoupling solutions increase the component stress and design complexity of the converter and transformer. In contrast, multiple algorithm-based decoupling solutions have also been proposed without modifying the circuit hardware topology. A widely adopted one is to introduce the inverse matrix of the MIMO model to suppress the cross-coupling between the single SISO control loops. Based on this natural idea, various advanced SISO control methods have been developed [6], [7], [8]. As the number of converter ports increases, these algorithm-based solutions may face increasing design complexity since the number of SISO controllers and the dimension of the inverse matrix will expand accordingly.

Besides, several MIMO control solutions for the MAB converters have also been reported. An artificial neural network was applied to calculate the optimal duty cycle of a triple-active-bridge converter [9]. A feedforward neural network was developed to predict the control variables required to achieve the target power flow [10]. These data-driven solutions determine the control actions in an open-loop manner. Therefore, feedback controllers in the outer loops are still required to ensure stability. A model predictive control (MPC) has also been proposed as a MIMO controller, in which an explicit control law is derived based on solving an optimization problem offline [11]. However, it lacks the ability to handle input and output constraints. In particular, incorporating output constraints is critical to achieve a safe and reliable operation. For instance, it prevents large voltage peaks during transients, which could trigger under voltage/over voltage lockout of connected devices or even cause component damage or failure [12]. It is worth noting that this aspect has not been discussed in the above-mentioned literature. At the same time, MPC has been applied to dual-active-bridge (DAB) converters (i.e., converters with two ports) to minimize current stress and transient dc offset, where its constrained optimization problem can be solved offline using the Karush–Kuhn–Tucker conditions [13], [14], [15]. However, as the number of variables and constraints increases substantially in the MAB converters, it becomes increasingly difficult to obtain an analytical solution offline.

In the field of power electronics, MPC has become increasingly popular in the past decade. It can be classified into two categories, namely finite-control-set MPC (FCS-MPC) and continuous-control-set MPC (CCS-MPC) [16]. FCS-MPC directly determines the optimal switching signals by enumerating the predicted behavior of all possible states, thereby eliminating the need for an external modulator. Due to its intuitive concept and straightforward implementation, it is widely used in the control of motor drives and grid-tied inverters [17]. In contrast, CCS-MPC solves a quadratic programming (QP) problem to obtain optimal control variables, which are then converted into switching signals through a modulator, such as carrier-based PWM or space vector PWM [16]. Input and output constraints can be included when formulating the QP problem. However, solving the QP problem in real time is particularly challenging due to its large computational burden and short sampling time of power converters. Compared to FCS-MPC, CCS-MPC remains unexplored in many power electronics applications.

As summarized in Table I, in recent years, a variety of CCS-MPC schemes based on optimization solvers, mostly the open-source qpOASES, have been reported for motor drives and neutral-point clamped converters [18], [19], [20], [21], [22], [23], [24], [25], [26]. However, most of the reported CCS-MPC implementations rely on high-performance but bulky platforms, such as dSPACE MicroLabBox or industrial computers, with processor speeds up to several GHz. Note that all the references cited in Table I included experimental validation. For the on-site applications of the MAB converters, such as multiport energy routers, it is important to reflect practical constraints and achieve a short sampling time with a low-cost embedded control platform, such as a microcontroller unit (MCU). A systematic effort on the constrained MPC problem formulation and fast real-time implementation is highly expected, particularly for the MAB converters. Therefore, this article aims to develop a new CCS-MPC scheme with over/under voltage protection (OVP/UVP) capability for MIMO control of the MAB converters and implement it in real-time on a low-cost MCU as fast as possible. The main contributions of this article include the following:

1) A systematic CCS-MPC MIMO control scheme for the MAB converters that include necessary input and output constraints required for OVP/UVP purposes.
2) A low-cost and fast implementation of the developed CCS-MPC control, including a new QP solver OSQP deployment and real-time certification.

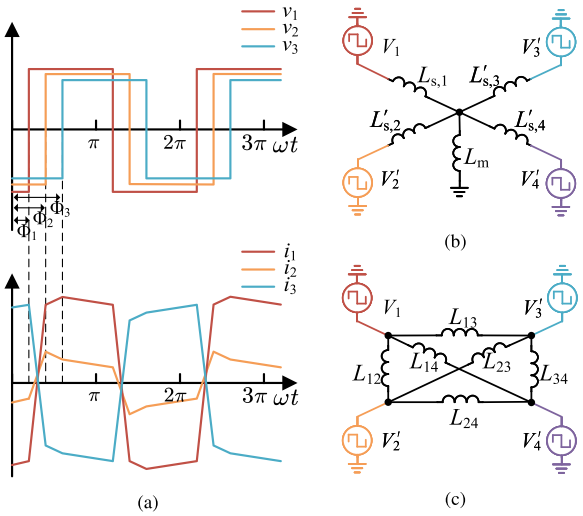

Fig. 2. Waveforms and equivalent circuits of an MAB converter. (a) Voltage and current waveforms. (b) "Y-type" equivalent circuit. (c) "Δ-type" equivalent circuit.

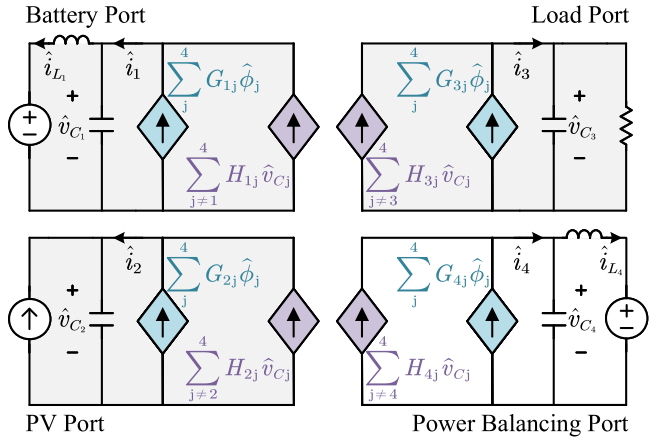

Fig. 3. Small signal model of the example four-port MAB converter.

3) A four-port prototype energy router with an embedded MPC controller running on a mainstream commercial MCU and demonstrating fast real-time implementation and OVP/UVP capability.

The rest of this article is organized as follows. Section II describes the formulation of CCS-MPC-based MIMO control problem, especially the reflection of the input and output constraints in the MAB converters; Section III focuses on the fast real-time implementation of the developed control scheme over a low-cost control platform, such as an MCU; Section IV gives simulation results as preliminary theoretical verification; Section V experimentally validates the control scheme and its real-time implementation using a prototype four-port energy router. Finally, Section VI concludes this article.

II. Problem Formulation

For the reliable operation of MAB converters, it is essential to satisfy practical constraints on both input and output variables. The theoretical aspects of the CCS-MPC problem formulation are first discussed, with particular emphasis on the handling of these practical constraints, which will guide the following low-cost real-time implementation.

A. Predictive Model

The CCS-MPC control of the MAB converters first requires a predictive model. Fig. 1 shows the topology of an example four-port MAB converter for energy routing purposes. The four H-bridge modules are driven by phase-shifted gate signals with a 50% duty cycle, generating square voltage waves with phase differences between each port. The piecewise-linear currents are then excited in the transformer windings, as shown in Fig. 2(a). Note that under the single-phase-shift modulation that dominates in the MAB converters, there are no other operation modes [1]. The power of each port of the MAB converter P_{i} can be expressed as follows:

$$P_{\mathrm{i}} = \sum_{\mathrm{j}\neq\mathrm{i}}^{4} \frac{V_{\mathrm{i}} V_{\mathrm{j}}}{2\pi f_{\mathrm{sw}} L_{\mathrm{ij}} N_{\mathrm{i}} N_{\mathrm{j}}} (\Phi_{\mathrm{i}} - \Phi_{\mathrm{j}}) \left(1 - \frac{|\Phi_{\mathrm{i}} - \Phi_{\mathrm{j}}|}{\pi}\right) \quad (1)$$

where f_{sw} is the switching frequency, V_{i}, N_{i}, and Φ_{i} are the dc voltage, number of transformer turns, and phase shift angle of the ith port, respectively. L_{ij} represents the link inductor between port i and j in the Δ-type equivalent circuit, which is calculated from the Y-type equivalent circuit, as shown in Fig. 2(b) and (c). The expressions of $L_{\mathrm{s,i}}$ and L_{ij} are defined in Appendix A.

Since the series inductor currents and series capacitor voltage consist of pure ac components with zero average value, these series components ($L_{\mathrm{s,1\text{-}4}}$ and $C_{\mathrm{s,1\text{-}4}}$) are ignored in the small signal model based on the reduced-order method. This simplification has demonstrated high accuracy in similar applications, such as the DAB converters [27]. Fig. 3 shows the small signal model of the above-mentioned four-port MAB converter, in which G_{ij} and H_{ij} are the small signal gains from port j to port i, referring to Appendix B [2], [11]. The connected sources/loads, i.e., the battery, PV panel, and dc load, are modeled as voltage source, current source, and resistive load, respectively. Here, the fourth port is designated as a power balancing port, whose phase shift angle is constantly zero to provide a reference. Based on the small signal model in Fig. 3, a MIMO predictive model can then be derived in the form of state–space equations

$$\begin{aligned} \dot{\boldsymbol{x}} &= A\boldsymbol{x} + B\boldsymbol{u} \\ \boldsymbol{y} &= C\boldsymbol{x} \end{aligned} \quad (2)$$

where state variables $\boldsymbol{x}$ are the states of storage components (i.e., dc inductor currents $\hat{i}_{L_1}$ and dc capacitor voltages $\hat{v}_{C_1}, \hat{v}_{C_2}, \hat{v}_{C_3}$); input variables (or control variables) $\boldsymbol{u}$ are the phase shift angles of the first three ports ($\hat{\phi}_1, \hat{\phi}_2, \hat{\phi}_3$); and battery current ($\hat{i}_{L_1}$), PV panel voltage ($\hat{v}_{C_2}$), and load voltage ($\hat{v}_{C_3}$) are chosen as three output variables, namely control targets

$$\begin{aligned} \boldsymbol{x} &= [x_1, x_2, x_3, x_4]^{\mathrm{T}} = \left[\hat{i}_{L_1}, \hat{v}_{C_1}, \hat{v}_{C_2}, \hat{v}_{C_3}\right]^{\mathrm{T}} \\ \boldsymbol{u} &= [u_1, u_2, u_3]^{\mathrm{T}} = \left[\hat{\phi}_1, \hat{\phi}_2, \hat{\phi}_3\right]^{\mathrm{T}} \\ \boldsymbol{y} &= [y_1, y_2, y_3]^{\mathrm{T}} = \left[\hat{i}_{L_1}, \hat{v}_{C_2}, \hat{v}_{C_3}\right]^{\mathrm{T}}. \end{aligned} \quad (3)$$

Note that since batteries operate in constant current (CC) mode most of the time, here the battery current is specifically chosen as an output variable [28]. System matrices $\{A, B, C\}$

in (2) are derived based on the Kirchhoff's law

$$A=\begin{bmatrix} 0 & 1/L_1 & 0 & 0 \\ -1/C_1 & 0 & H_{12}/C_1 & H_{13}/C_1 \\ 0 & H_{21}/C_2 & 0 & H_{23}/C_2 \\ 0 & H_{31}/C_3 & H_{32}/C_3 & -1/(C_3R_3) \end{bmatrix}$$

$$B=\begin{bmatrix} 0 & 0 & 0 \\ G_{11}/C_1 & G_{12}/C_1 & G_{13}/C_1 \\ G_{21}/C_2 & G_{22}/C_2 & G_{23}/C_2 \\ G_{31}/C_3 & G_{32}/C_3 & G_{33}/C_3 \end{bmatrix}$$

$$C=\begin{bmatrix} 1 & 0 & 0 & 0 \\ 0 & 0 & 1 & 0 \\ 0 & 0 & 0 & 1 \end{bmatrix}. \tag{4}$$

For a digital implementation, the continuous-time predictive model (2) must be discretized with sampling time T_s, such as through exact discretization method

$$\begin{aligned} \Delta \boldsymbol{x}(k+1) &= G\Delta \boldsymbol{x}(k) + H\Delta \boldsymbol{u}(k) \\ \Delta \boldsymbol{y}(k) &= C\Delta \boldsymbol{x}(k) \end{aligned} \tag{5}$$

where $G=e^{AT_s}$, $H=(\int_0^{T_s} e^{A\tau}d\tau)B$, and $\Delta = 1-z^{-1}$ is a difference operator. Thus, the output variables at the next j step, $\vec{\boldsymbol{y}}(k+j|k)$ can be predicted in an iterative manner. Here, the vector form of the predicted output variables within a predictive horizon N_p, denoted as $\vec{\boldsymbol{Y}}(k)$, is expressed as follows:

$$\begin{aligned} \vec{\boldsymbol{Y}}(k) &= \left[\vec{\boldsymbol{y}}(k+1|k)^\mathrm{T}\ \vec{\boldsymbol{y}}(k+2|k)^\mathrm{T}\cdots \vec{\boldsymbol{y}}(k+N_\mathrm{p}|k)^\mathrm{T}\right]^\mathrm{T} \\ &= L\Delta \boldsymbol{U}(k) + F\Delta \boldsymbol{x}(k) + \boldsymbol{Y}_0(k) \end{aligned} \tag{6}$$

where matrices L and F are defined in Appendix C, and $\boldsymbol{Y}_0(k)$ and $\Delta \boldsymbol{U}(k)$ are vectors of present output variables and assumed control increments along the predictive horizon, respectively

$$\begin{aligned} \boldsymbol{Y}_0(k) &= \left[\boldsymbol{y}(k)^\mathrm{T}\ \boldsymbol{y}(k)^\mathrm{T}\ \ldots\ \boldsymbol{y}(k)^\mathrm{T}\right]^\mathrm{T} \\ \Delta \boldsymbol{U}(k) &= \left[\Delta \boldsymbol{u}(k)^\mathrm{T}\ \Delta \boldsymbol{u}(k+1)^\mathrm{T}\cdots \Delta \boldsymbol{u}(k+N_\mathrm{p}-1)^\mathrm{T}\right]^\mathrm{T}. \end{aligned} \tag{7}$$

B. Formulation of Constrained CCS-MPC Problem

The MPC controller needs to solve an optimization problem online within each sampling interval to obtain a control action $\Delta \boldsymbol{u}^*(k)$. Here, the cost function J of the optimization problem is defined as the weighted sum of squares of predicted errors and control increments along the horizon N_p, namely

$$J=\sum_{i=1}^{N_\mathrm{p}} \|\vec{\boldsymbol{y}}(k+i)-\boldsymbol{w}(k+i)\|_Q^2 + \|\Delta \boldsymbol{u}(k+i-1)\|_R^2 \tag{8}$$

where $\vec{\boldsymbol{y}}(k+i)$, $\boldsymbol{w}(k+i)$, and $\Delta \boldsymbol{u}(k+i)$ are the predicted outputs, output references, and control increments at the next i step, respectively. Q and R are weighting factor matrices of the predicted errors and control increments (refer to Appendix D).

In the deadbeat predictive control, the analytical solution of the optimization problem is derived offline by directly solving $\mathrm{d}J/\mathrm{d}\Delta \boldsymbol{U}(k)=0$, neglecting the constraints on input and output variables [11]. However, the developed CCS-MPC scheme here

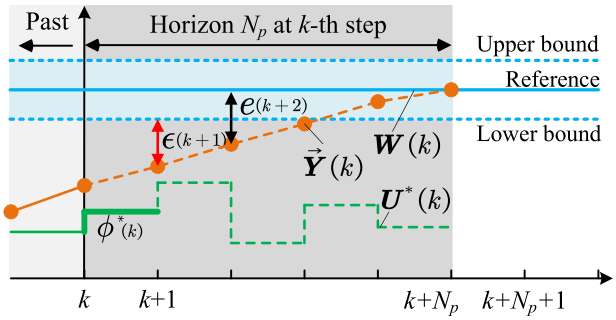

Fig. 4. Illustration of soft constraint on output variables at kth instant.

for the MAB converters further incorporates constraints on both input and output variables. First, the phase shift angles of MAB converters must be strictly bounded within a range of $[-\pi/2, \pi/2]$ to guarantee a monotonic relationship between the output power and phase shift angle at each port [refer to P_i in (1)]. This requires a hard constraint imposed on the control variables $\boldsymbol{u}$ over the predictive horizon N_p

$$-\pi/2 \le \boldsymbol{u}(k+i) \le \pi/2, \quad i \in (0, N_\mathrm{p}-1). \tag{9}$$

At the same time, to ensure safety operation and protection, constraints on the output variables should also be reflected over the horizon N_p. For instance, constraints on the dc load voltage $\vec{y}_3$ are imposed as

$$V_{\mathrm{load,min}} \le \vec{y}_3(k+i) \le V_{\mathrm{load,max}}, \quad i \in (1, N_\mathrm{p}). \tag{10}$$

But if these output constraints are imposed as strict boundaries that can never be violated, the optimization problem itself may become infeasible [29]. To address this challenge, such constraints have to be softened in practical applications, permitting occasional violations only when really necessary. A possible solution is to introduce a nonnegative slack variable ϵ. This variable particularly represents the degree of constraint violation, For instance, $\epsilon(k+1)$ in Fig. 4 is the quantities of constraint violation of $\vec{y}(k+1)$. This slack variable ϵ should be penalized in the cost function J, forcing its value to be as close to zero as possible. As an example, the constraint on the dc load voltage in (10) can be softened as

$$\begin{aligned} V_{\mathrm{load,min}} - \epsilon_3(k+i) \le \vec{y}_3(k+i) \le V_{\mathrm{load,max}} + \epsilon_3(k+i) \\ \epsilon_3(k+i) \ge 0. \end{aligned} \tag{11}$$

Without loss of generality, constraints on the other output variables, i.e., battery current and PV panel voltage, are similarly introduced and softened. Although they are relatively less restrictive in the present application, as discussed further in Section IV. These soft constraints on the output variables at time instant $k+i$ can be rearranged in a vector form

$$K\boldsymbol{\epsilon}(k+i) \ge M\vec{\boldsymbol{y}}(k+i) + \boldsymbol{c} \tag{12}$$

where $\boldsymbol{\epsilon}(k+i)=[\epsilon_1(k+i), \epsilon_2(k+i), \epsilon_3(k+i)]$ is the vector of slack variables, and matrix K, M, and vector $\boldsymbol{c}$ are defined in Appendix E.

As explained previously, to avoid the violation of these output constraints in (12) as much as possible, a quadratic penalty for slack variables $\|\boldsymbol{\epsilon}(k+i)\|_S^2$ can be added into the cost function J, where S is the weighting matrix of slack variables:

$S = \text{diag}\{s_1, s_2, s_3\}$. Then, a final optimization problem is formulated as follows:

$$\begin{aligned}\min_{\Delta \boldsymbol{u},\boldsymbol{\epsilon}} J = &\sum_{i=1}^{N_\text{p}} \|\vec{\boldsymbol{y}}(k+i) - \boldsymbol{w}(k+i)\|_Q^2 \\ &+ \|\Delta \boldsymbol{u}(k+i-1)\|_R^2 + \|\boldsymbol{\epsilon}(k+i)\|_S^2 \\ \text{s.t.}\quad &\Delta \boldsymbol{x}(k+i+1) = G\Delta \boldsymbol{x}(k+i) + H\Delta \boldsymbol{u}(k+i) \\ &\Delta \boldsymbol{y}(k+i) = C\Delta \boldsymbol{x}(k+i) \\ &\Delta \boldsymbol{u}(k+i) = \boldsymbol{u}(k+i) - \boldsymbol{u}(k+i-1) \\ &-\pi/2 \le \boldsymbol{u}(k+i-1) \le \pi/2 \\ &K\boldsymbol{\epsilon}(k+i) \ge M\vec{\boldsymbol{y}}(k+i) + \boldsymbol{c} \\ &i \in (1, N_\text{p}). \end{aligned} \tag{13}$$

The above-mentioned optimization problem in (13) is solved at each time instant to obtain an optimal control sequence $\Delta \boldsymbol{U}^*(k)$. In this control sequence, only the optimal control variable at present time instant $\Delta \boldsymbol{u}^*(k)$ is actually implemented [29]

$$\Delta \boldsymbol{u}^*(k) = [\boldsymbol{I}_3, \boldsymbol{0}_3, \ldots, \boldsymbol{0}_3]\, \Delta \boldsymbol{U}^*(k) \tag{14}$$

where $\boldsymbol{I}_3$ and $\boldsymbol{0}_3$ are 3×3 identity matrix and zero matrix, respectively. At the next time instant, the horizon N_p recedes by one step, and the above-mentioned optimization is repeated based on new measurements. Note that the above-mentioned MPC problem is formulated in an incremental structure, which implicitly integrates tracking errors and thus ensures the steady-state accuracy.

III. Low-Cost Implementation

As mentioned in the introduction section, solving the optimization problem (13) online within a short sampling interval is quite computationally challenging. To realize real-time implementation of the above-mentioned developed CCS-MPC scheme on a low-cost control platform, such as MCUs, the following three aspects are especially discussed, including 1) problem reformulation, 2) solver selection, and 3) modification for real-time certification.

A. Conversion to a QP Problem

Due to the quadratic form of the cost function J, the optimization problem in (13) can be converted to a condensed QP form, which is more efficient for the embedded implementation. Similar to the representation of $\vec{\boldsymbol{Y}}(k)$ and $\Delta \boldsymbol{U}(k)$ in (7), the control variables, slack variables, and output references along the predictive horizon N_p can all be represented by a vector form

$$\begin{aligned}\boldsymbol{U}(k) &= \left[\boldsymbol{u}(k)^\text{T}\, \boldsymbol{u}(k+1)^\text{T} \cdots \boldsymbol{u}(k+N_\text{p}-1)^\text{T}\right]^\text{T} \\ \boldsymbol{E}(k) &= \left[\boldsymbol{\epsilon}(k+1)^\text{T}\, \boldsymbol{\epsilon}(k+2)^\text{T} \cdots \boldsymbol{\epsilon}(k+N_\text{p})^\text{T}\right]^\text{T} \\ \boldsymbol{W}(k) &= \left[\boldsymbol{w}(k+1)^\text{T}\, \boldsymbol{w}(k+2)^\text{T} \cdots \boldsymbol{w}(k+N_\text{p})^\text{T}\right]^\text{T}.\end{aligned}$$

Then, the cost function J in (13) can also be converted to a compact vector form through a few algebraic manipulations

$$\begin{aligned}J = &\left[\vec{\boldsymbol{Y}}(k) - \boldsymbol{W}(k)\right]^\text{T} \mathcal{Q} \left[\vec{\boldsymbol{Y}}(k) - \boldsymbol{W}(k)\right] \\ &+ \Delta \boldsymbol{U}(k)^\text{T} \mathcal{R} \Delta \boldsymbol{U}(k) + \boldsymbol{E}(k)^\text{T} \mathcal{S} \boldsymbol{E}(k).\end{aligned} \tag{15}$$

Accordingly, based on the definition of $\boldsymbol{E}(k)$ and $\vec{\boldsymbol{Y}}(k)$, the soft constraints (12) along the predictive horizon N_p is modified as

$$\mathcal{K}\boldsymbol{E}(k) \ge \mathcal{M}\vec{\boldsymbol{Y}}(k) + \bar{\boldsymbol{c}} \tag{16}$$

where $\mathcal{Q}$, $\mathcal{R}$, and $\mathcal{S}$ are block diagonal matrices of weighting matrices Q, R, and S, while $\mathcal{K}$ and $\mathcal{M}$ are block diagonal matrices of K and M. The detailed expressions of these matrices and vector $\bar{\boldsymbol{c}}$ are defined in Appendix F.

Similarly, since the optimization variables in (13) are control increments $\Delta \boldsymbol{U}(k)$, the hard constraints (9) on the phase shift angles $\boldsymbol{U}(k)$ should also be modified with respect to $\Delta \boldsymbol{U}(k)$

$$-\pi/2 - \boldsymbol{U}_0(k-1) \le \mathcal{N}\Delta \boldsymbol{U}(k) \le \pi/2 - \boldsymbol{U}_0(k-1) \tag{17}$$

where $\mathcal{N}$ are defined in Appendix F, and $\boldsymbol{U}_0(k-1)$ is the vector of control variables employed at previous time instance $k-1$

$$\boldsymbol{U}_0(k-1) = \left[\boldsymbol{u}(k-1)^\text{T}\, \boldsymbol{u}(k-1)^\text{T} \cdots \boldsymbol{u}(k-1)^\text{T}\right]^\text{T}.$$

As mentioned previously, the slack variables $\boldsymbol{E}(k)$ is augmented into the optimization variables, i.e., $\Delta \tilde{\boldsymbol{U}}(k) = [\Delta \boldsymbol{U}(k)^\text{T}, \boldsymbol{E}(k)^\text{T}]^\text{T}$. Then, by substituting $\vec{\boldsymbol{Y}}(k)$ in the modified cost function (15) and soft constraints (16) with the expression in (6), the original optimization problem can be converted to a QP problem with respect to the augmented optimization variables $\Delta \tilde{\boldsymbol{U}}(k)$

$$\begin{aligned}\min_{\Delta \tilde{\boldsymbol{U}}(k)}\ & J = \Delta \tilde{\boldsymbol{U}}(k)^\text{T} P \Delta \tilde{\boldsymbol{U}}(k) + 2q\Delta \tilde{\boldsymbol{U}}(k) \\ \text{s.t.}\ & lb \le \mathcal{A}\Delta \tilde{\boldsymbol{U}}(k) \le ub\end{aligned} \tag{18}$$

where the quadratic cost matrix P, linear cost vector q, constraint matrix $\mathcal{A}$, lower bound lb, and upper bound ub are defined as follows:

$$\begin{aligned}P &= \begin{bmatrix} L^\text{T}\mathcal{Q}L + \mathcal{R} & \boldsymbol{0}_{3N_\text{p}} \\ \boldsymbol{0}_{3N_\text{p}} & \mathcal{S}\end{bmatrix} \quad \mathcal{A} = \begin{bmatrix} \mathcal{N} & \boldsymbol{0}_{3N_\text{p}} \\ \mathcal{M}L & -\mathcal{K}\end{bmatrix} \\ q &= \left[\left[F\Delta \boldsymbol{x}(k) + \boldsymbol{Y}_0(k) - \boldsymbol{W}(k)\right]^\text{T} \mathcal{Q}L,\ \boldsymbol{0}_{1\times 3N_\text{p}}\right] \\ lb &= \left[\left[-\frac{\pi}{2} - \boldsymbol{U}_0(k-1)\right]^\text{T}, [-\boldsymbol{\infty}_{1\times 9N_\text{p}}]^\text{T}\right]^\text{T} \\ ub &= \left[\left[\frac{\pi}{2} - \boldsymbol{U}_0(k-1)\right]^\text{T}, [-\mathcal{M}F\Delta \boldsymbol{x}(k) - \mathcal{M}\boldsymbol{Y}_0(k) - \bar{\boldsymbol{c}}]^\text{T}\right]^\text{T}.\end{aligned} \tag{19}$$

Note that $\boldsymbol{0}_{1\times 3N_\text{p}}$ represents a zero row vector with a dimension of $3N_\text{p}$.

B. Embedded Platform and Solver

The above-mentioned converted QP problem should be solved at each sampling instant. Benefiting from the development of numerical solvers in recent years, a variety of open source and commercial QP solvers have been developed and successfully deployed in the MPC applications. The most popular QP solver in the field of power electronics is `qpOASES`, which can solve QP problems in a range of hundreds of microseconds and has a user-friendly interface for Simulink and dSPACE MicroLabBox [30]. For instance, most reported motor drive CCS-MPC schemes deployed the QP solver `qpOASES` on dSPACE MicroLabBox for real-time implementation [18], [19], [20], [21].

However, in actual applications, it is usually desirable to realize a low-cost embedded implementation of the developed

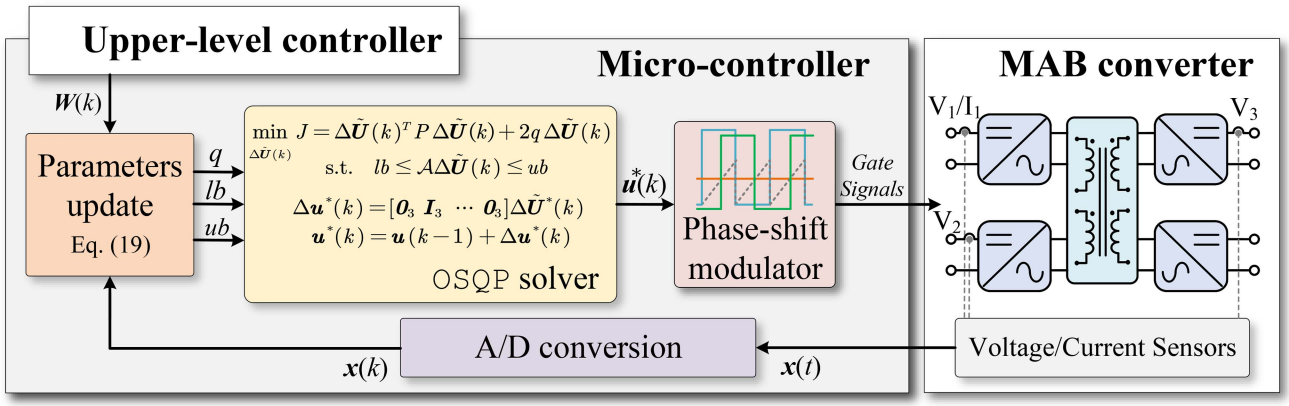

Fig. 5. Control diagram of the developed CCS-MPC scheme for MAB converters.

CCS-MPC schemes, such as on a commercial MCU. Here, a new QP solver OSQP is applied to solve the problem (18) in real-time, which is based on the efficient alternating direction method of multipliers (ADMMs) [31]. The ADMM is particularly effective for large-scale QP problems with multiple constraints, such as (18). It decomposes a complex problem into simpler subproblems that can be solved more efficiently. In contrast, the classical active set (AS) method in qpOASES requires frequent re-evaluation of the active constraints, which may become inefficient when dealing with a large number of constraints. The code generation tool of OSQP also makes it particularly suitable for the present low-cost embedded implementation problem, as it can generate compact C codes for a specific QP problem [32].

Fig. 5 shows the control diagram of the developed CCS-MPC scheme for the MAB converters. As a core of the control scheme, OSQP is responsible for solving the QP problem with varying input parameters at each time instant, namely q, lb, and ub. From (19), it can be seen that the quadratic cost matrix P and constraint matrix $\mathcal{A}$ remain unchanged at different time instants. The varying parameters q, lb, and ub depend on the real-time measured voltages and currents [i.e., $\Delta\boldsymbol{x}(k)$ and $\boldsymbol{Y}_0(k)$], thereby need to be constantly updated before the QP solving. This makes the problem in (18) a parametric program, as required by the QSQP solver. The matrices P and $\mathcal{A}$ can be precomputed offline to accelerate the implementation of the solver, and the resulting algorithm is division-free [32]. As shown in Fig. 5, with the updated input parameters, OSQP solves the optimal control variables $\Delta\boldsymbol{u}^*(k)$ and sends them to the phase-shift modulator to generate gate signals.

C. Real-Time Certification and Delay Compensation

In the OSQP solver, determining the optimal control variables $\Delta\tilde{\boldsymbol{U}}(k)$ requires multiple ADMM iterations. The number of iterations depends on multiple factors, including the size of the QP problem, initial iteration point, and convergence tolerance level. By default, the iteration process terminates once the computed residual falls below a specified tolerance level, i.e., the convergency. However, this termination criterion leads to a varying iteration number and execution duration at different time instants, which may cause the MPC execution duration T_{mpc} to exceed an expected sampling interval T_{s}, thereby violating the real-time requirement, as shown in Fig. 6(a). The worst-case

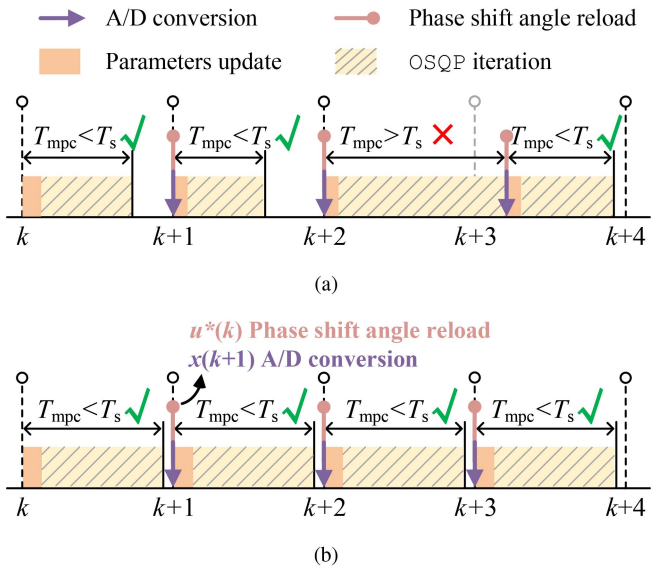

Fig. 6. Graphical description of the MPC implementation. (a) Without real-time certification. (b) With real-time certification.

execution duration has been checked to ensure that the selected sampling interval is always longer than this worse-case duration, namely in a case-by-case manner [21], [25], [26].

For a strict real-time certification, a new termination criterion is proposed here. Instead of iterating continuously until the residual falls below its tolerance level, the solver fully utilizes the available sampling interval T_{s} for the iterative computations, and terminates the iteration when T_{mpc} approaches T_{s}, as shown in Fig. 6(b). Although this new criterion may slightly sacrifice the accuracy and convergence of results, it guarantees the feasibility of real-time implementation, which is more important in the present application of MPC control. Once the QP problem is formulated, T_{mpc} can be largely determined by the number of iterations, as parameter updates typically have a fixed execution duration. Therefore, the proposed termination criterion can be straightforwardly implemented by adjusting the maximum number of iterations in OSQP solver, ensuring that the resulting T_{mpc} fits within T_{s}. In addition, because OSQP is a numerical solver,

TABLE II
SOFT CONSTRAINTS ON OUTPUT VARIABLES

Parameter and symbol	Rated value	Min.	Max.
DC loads voltage V_{load}	48 V	**44 V**	**52 V**
PV panel voltage V_{pv}	48 V	0 V	60 V
Battery current I_{bat}	3 A	−6 A	6 A

TABLE III
SPECIFICATIONS OF PROTOTYPING ENERGY ROUTER

Module	Parameter and symbol	Specification
Power modules	MOSFET	HSBA15810C
	Port voltage V_{i}	48 V
	Port inductor L_{i}	15 μH
	Port capacitor C_{i}	680 μF
	Series inductor $L_{\text{s,i}}$	2.2 μH
	Series capacitor $C_{\text{s,i}}$	200 μF
	Switching frequency f_{sw}	100 kHz
	Deadtime t_{d}	66 ns
Planar transformer	Turns ratio N_{i}	4:4:4:4 Nt
	PCB winding width	20 mm
	PCB winding thickness	70 μm (2 oz)
	Magnetic core type	DMEGC EIW58.4A
	Magnetic core material	DMEGC DMR95
Sampling modules	Optical isolator	ACPL-C87H
	Hall sensor	TMCS1100
	Operational amplifier	MAX44245
MPC controller	MCU	STM32H723VGT6
	Sampling time T_{s}	200 μs
	Horizon length N_{p}	3
	Weighting matrix Q	$\text{diag}\{\frac{1}{(4\text{A})^2}, \frac{1}{(48\text{V})^2}, \frac{1}{(48\text{V})^2}\}$
	Weighting matrix S	$\text{diag}\{\frac{1}{\text{A}^2}, \frac{1}{\text{V}^2}, \frac{1}{\text{V}^2}\} \cdot 0.005$
	Weighting matrix R	$\text{diag}\{1, 1, 1\} \cdot 500/\text{rad}^2$

control stability itself is determined by the MPC controller parameters including the horizon length N_{p} and weighting matrices Q, R, and S [29].

Meanwhile, the computed control action will be executed at the beginning of next sampling interval under this criterion, as shown in Fig. 6(b), which will introduce an execution delay of T_{s}. To compensate for this one-step delay, the discrete predictive model (5) is modified accordingly as

$$\Delta \boldsymbol{x}\,(k+1) = G\Delta \boldsymbol{x}(k) + H\Delta \boldsymbol{u}\,(k-1)\,. \tag{20}$$

The executed optimal control variables in (14) are then adjusted as

$$\Delta \boldsymbol{u}^*(k) = [\boldsymbol{0}_3, \boldsymbol{I}_3, \ldots, \boldsymbol{0}_3]\,\Delta\tilde{\boldsymbol{U}}^*(k). \tag{21}$$

IV. PARAMETER DESIGN AND SIMULATION

The effectiveness of the developed CCS-MPC scheme for the MAB converters, featuring OVP/UVP, is first verified through simulations on PLECS software. The four-port circuit topology and parameters are identical to those of the following experimental prototype, as detailed in Fig. 1 and Table III. The choice of N_{p} and T_{s} is particularly crucial for real-time implementation and will be further discussed in the following section on experimental validation. The weighting matrix Q for predicted errors is designed to normalize the different terms in the cost function, as defined in Appendix D. The weighting matrices R and S for control increments and slack variables are tuned through the branch-and-bound (BnB) method to prevent aggressive actions and ensure stability [33].

The constraint on dc load voltage is set within ± 4 V of its rated value (i.e., $[44\,\text{V}, 52\,\text{V}]$), which is a strict constraint because of the narrow range of allowed load voltage variation and possible sudden load change. The upper bound of PV panel voltage is specified as its open-circuit voltage (i.e., 60 V), which is approximately 1.3 times the operation voltage, indicating a wide permitting voltage range [34]. And the maximum permissible battery current is ± 6 A. Due to the presence of a filter inductor in the battery port, which is a common practice for current-fed ports, this port is unlikely to experience current overshoot and undershoot [35]. Therefore, the two constraints on the PV panel voltage and battery current are less restrictive than the constraint on the dc load voltage. The above-mentioned three soft constraints [i.e., $\boldsymbol{c}$ in (12) and Appendix E] on the output variables are further summarized in Table II.

The weighting factors on constraint violations $\boldsymbol{\epsilon}$ are uniformly defined as $S = \text{diag}\{s, s, s\}$, and their impact is discussed as follows. A dynamic link library (DLL) file is developed using the `OSQP` solver through the visual studio integrated development environment. This DLL file is then called via the PLECS DLL block and used as a digital controller in the simulation. Fig. 7 shows the simulated waveforms of the MAB converter under the MPC control with/without OVP/UVP and with different uniform weighting factor s. Here, the load at port #3 undergoes a step change, dropping from 48 to 19.2 Ω at 0.4 s, and returning to 48 Ω at 0.6 s. Under the MPC control without OVP/UVP (i.e., $s = 0$), the voltage overshoot/undershoot during the transient responses significantly exceeds the constraint, which is indicated by the gray area in Fig. 7. However, once the constraint violations are penalized (i.e., $s > 0$), the overshoot and undershoot are effectively suppressed. Increasing the weighting factor s results in reduced constraint violations. However, a tradeoff in the value of s exists between the constraint violation penalty and control stability. In practice, s is tuned via the BnB method to minimize constraint violations while avoiding oscillatory responses (i.e., poor stability).

V. EXPERIMENTAL RESULTS

A. Prototype and Experimental Setup

A four-port MAB converter, working as an energy router, is fabricated in house for experimental validation, as shown in Fig. 8. The above-mentioned constrained CCS-MPC scheme is implemented on a low-cost control platform, an STM32H723 MCU (Arm Cortex-M7 with 550 MHz clock and floating-point unit). This MCU, which costs about ten USDs, performs A/D conversion (12-bit resolution), QP problem solving through the `OSQP` solver, and phase-shifted gate signal modulation (refer to Fig. 5). The state variables $\boldsymbol{x}$, namely the dc voltages and currents, are measured through optical isolators and Hall sensors. High-precision components, calibration, and A/D oversampling are especially adopted to minimize measurement and quantization noise. The detailed parameters and specifications of the above-mentioned prototyping energy router are listed in Table III. Here, the switching frequency and series inductance are determined according to (1) to meet the required power level. The series capacitance is chosen to be large enough to block the dc bias, and the dead time is tuned to achieve full zero voltage switching (ZVS). The transformer turns ratio is designed

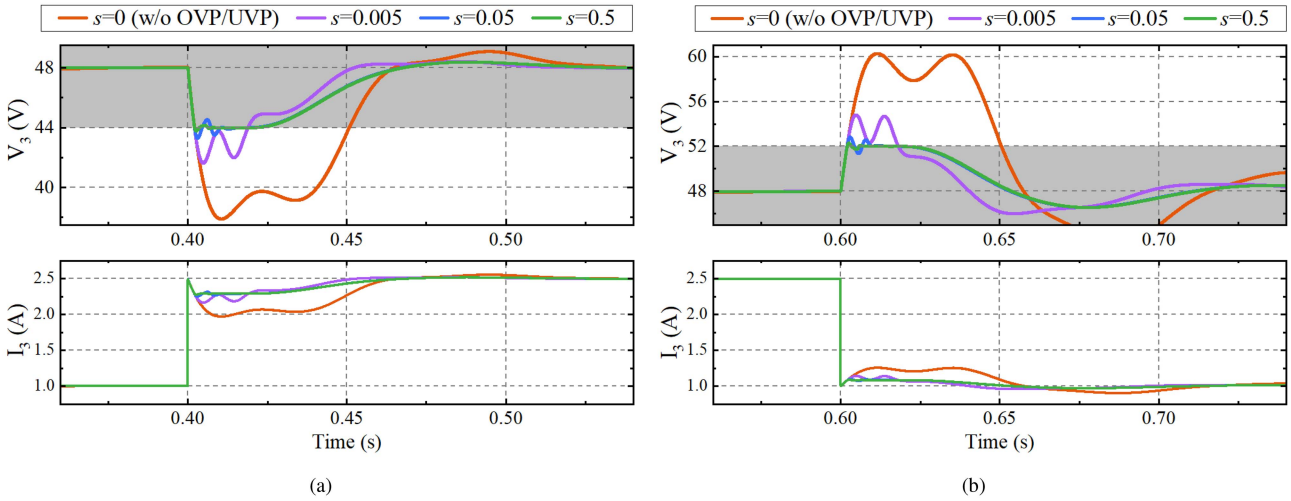

Fig. 7. Simulated waveforms with different weighting factors (i.e., s) on constraint violations. (a) Load change in port #3 from 48 to 19.2 Ω at 0.4 s. (b) Load change in port #3 from 19.2 to 48 Ω at 0.6 s.

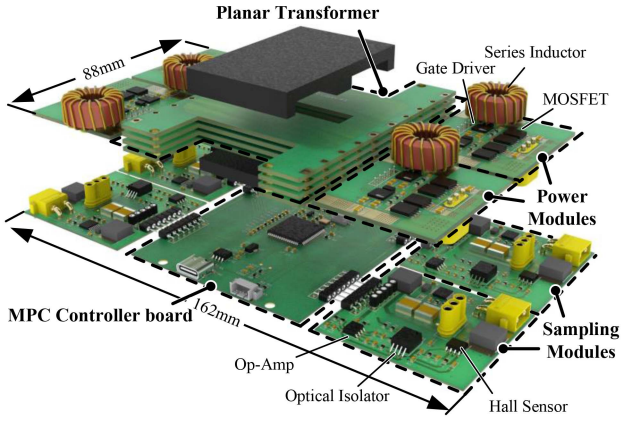

Fig. 8. 3-D assembly drawing of the prototyping four-port energy router.

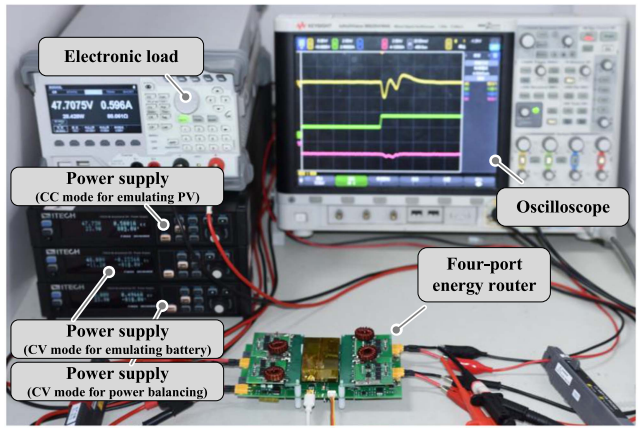

Fig. 9. Laboratory experimental setup.

to match the port voltage ratio, ensuring full-range soft switching for all the H-bridges [36].

Fig. 9 shows the entire laboratory experimental setup. Here, ports #1 and #4 of the four-port prototyping energy router are connected to their respective bidirectional power supplies both configured in constant voltage mode for emulating the storage battery and power balancing, while port #2 is connected to another power supply configured in CC mode emulating the PV panels, and port #3 is connected to a programmable electronic load as a dc load. Note that in this article (including in the following experiments), the dc–ac function (i.e., the dc–ac converter in Fig. 1) is not considered. The host PC transmits the reference voltage/current signal of each port, i.e., $\boldsymbol{W}(k)$, to the MCU via the UART protocol.

Fig. 10(a) illustrates the steady-state waveforms of the energy router. The turn-ON transient is especially enlarged to confirm the ZVS operation. Fig. 10(b) presents the power loss breakdown under full load condition. Fig. 11(a) shows the measured efficiency contours in a two-input two-output scenario, in which the PV port and battery port are configured as input ports, while the load port and power balancing port are configured as output ports

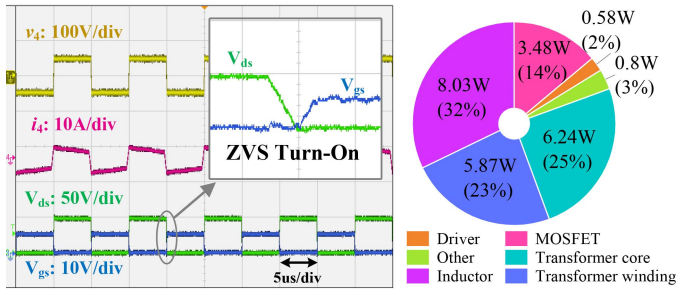

Fig. 10. Steady-state characteristics. (a) Voltage/current waveforms and ZVS characteristics. (b) Loss breakdown under a full load operating condition.

with the same output power. Fig. 11(b) summarizes the measured MIMO efficiency curves with different port configurations. The developed prototype can deliver a maximum power of 500 W. The peak efficiency is over 97% and the MIMO efficiency maintains above 95% across a wide operation range.

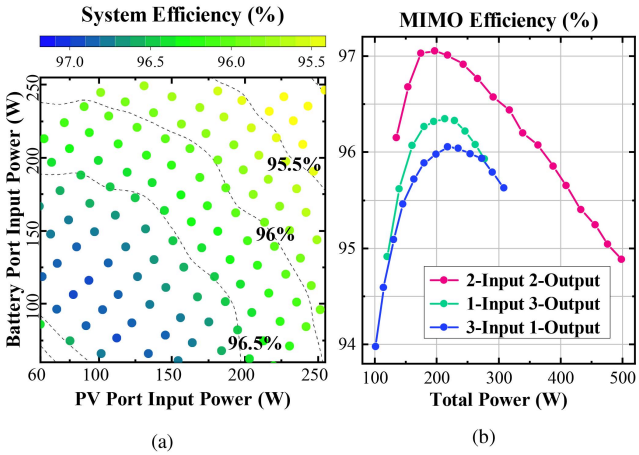

Fig. 11. Measured system efficiency. (a) Efficiency contours in a two-input two-output scenario. (b) MIMO efficiency curves with different port configurations.

B. Over/Under Voltage Protection

The dynamic performance of the developed MPC control with OVP/UVP is compared with that under the MPC control without OVP/UVP and conventional PI control. Note that under the MPC control without OVP/UVP, the constraints on output variables are invalid by setting the weighting factor $s = 0$, and the input constraints (9) are still effective. And under the PI control, input saturators and integrator clamping are applied in the following experiments, as the input/output constraints are difficult to explicitly incorporate. As examples, the dynamic responses to step load changes at port #3 under the three controls are shown in Figs. 12 and 13; and the dynamic responses under current reference change at port #1 are shown in Fig. 14.

The UVP capability of the constrained MPC control is first demonstrated by comparing the three waveforms in Fig. 12, where the dc load at port #3 is suddenly changed from 1 to 2.5 A. Fig. 12(b) and (c) shows that under MPC control without OVP/UVP and PI control, the voltage undershoot is as high as 7 and 7.5 V, respectively, which obviously exceeds the lower bound (represented by the straight yellow line). In contrast, the developed MPC control with OVP/UVP effectively suppresses this voltage undershoot, resulting in only minor constraint violation. As shown in Fig. 12(a), when the lower bound is at risk of being violated, the predicted slack variables $\boldsymbol{\epsilon}$ become positive, forcing the MPC control to adjust the phase shift angles that minimize the constraint violation [refer to (13)]. Fig. 13(a)–(c) shows the dynamic responses to a load change at port #3 from 2.5 A back to 1 A. Again, the OVP capability is confirmed as the voltage overshoot under the MPC control with OVP/UVP only slightly exceeds the upper bound, while the peak overshoot under the MPC control without OVP/UVP and PI control is more than one-third larger. Fig. 14(a)–(c) shows the dynamic responses to the current reference change of port #1 from 1 to –1.5 A under the three controllers. The waveforms of the two MPC controls in Fig. 14(a) and (b) are nearly identical, as no output constraints are violated during the transient process. Consequently, the MPC with OVP/UVP behaves equivalently to the MPC without OVP/UVP in this scenario, since the slack variables $\boldsymbol{\epsilon}$ are both zero. Meanwhile, under the PI control, V_3 in Fig. 14(c) exceeds the constraint due to the cross-coupling effect.

In addition, since the cross-coupling effect of the MAB converter can be explicitly reflected in the predictive model (refer to Section II-A), the interferences between the ports can be better suppressed through the MPC controls than through the PI control. For instance, in Fig. 14, the current reference (I_1) change at port #1 causes the output voltage (V_3) at port #3 to fluctuate, and the two MPC controls reduce the fluctuation in V_3 compared to the PI control. The similar results can also be observed in Figs. 12 and 13. Meanwhile, the fluctuations in I_1 under the MPC with OPV/UVP in Figs. 12(a) and 13(a) are not as same as the MPC without OPV/UVP in Figs. 12(b) and 13(b). This is because the MPC with OPV/UVP enforces stricter penalties on the constraint violations, which in turn reduces the effort allocated to current reference tracking in port #1. At the same time, the suppression of the output constraint violations also shortens the settling time of transient responses, as shown by comparing Fig. 12(a) and (b) as well as Fig. 13(a) and (b).

The robustness of the developed MPC is further checked by introducing parameter variations. Specifically, the series inductance at port #3 ($L_{s,3}$) varies by approximately $\pm 30\%$ (i.e., 1.5 and 3 μH) compared to its nominal value 2.2 μH. As shown in Fig. 15, the experimental results demonstrate that the MPC control can suppress the load disturbance and maintain stable performance despite the inductance variation. Fig. 16 illustrates the impact of the weighting factor s. It can be seen that increasing s reduces the constraint violation, but an excessively large s may degrade the control performance or even cause oscillatory responses (i.e., poor stability). As mentioned in Section IV, s(=0.005 here) is typically tuned via the BnB method to minimize constraint violations while avoiding oscillation [33].

C. Timing Analysis

To investigate the actual real-time performance, the execution duration of the developed CCS-MPC control in each time instant is measured by toggling a signal at the beginning and end of the control algorithm execution, as shown in Fig. 17. The total execution duration T_{mpc} (i.e., ③) is consistent at different time instants, which proves the above-mentioned theoretical analysis in Fig. 6(b) and thus the real-time certification.

It is worth noting that the consistent execution duration is the most notable advantage of the `OSQP` solver, as the problem dimension of the ADMM algorithm remains constant across iterations [31]. Consequently, once the number of iterations is specified, the execution duration becomes deterministic and consistent, providing a strict real-time certification. In contrast, the AS algorithm used in `qpOASES` exhibits a varying problem dimension across iterations, since a different number of constraints may be activated at each iteration. As a result, the total execution duration fluctuates even when the number of iterations is fixed. In practical applications, the sampling time T_s is typically chosen to be significantly longer than the worst-case execution duration to maintain a safety margin [18], [19], [20], [21].

The execution duration with different horizon lengths (N_{p}) and numbers of iterations (N_{iter}) under the proposed termination criterion in Section III-C is also examined to provide guidance for parameter selection, as shown in Fig. 18. Increasing N_{p} and N_{iter} results in a longer execution duration, thus requires a longer sampling time T_{s} for the present embedded implementation. Meanwhile, it is known that a larger N_{p} also enhances the control stability, and a larger N_{iter} increases the accuracy of optimization results [29]. Based on the experimental results in

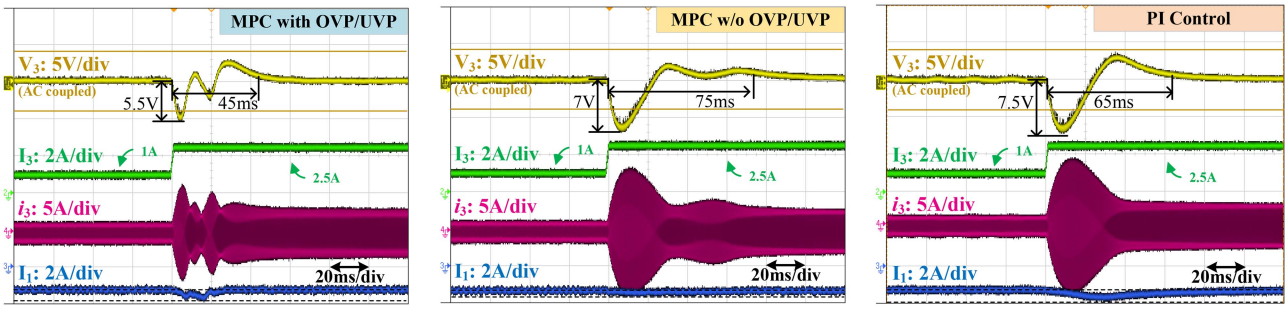

Fig. 12. Dynamic responses under a step load change at port #3 from 1 to 2.5 A. (a) MPC with OVP/UVP. (b) MPC without OVP/UVP. (c) PI control.

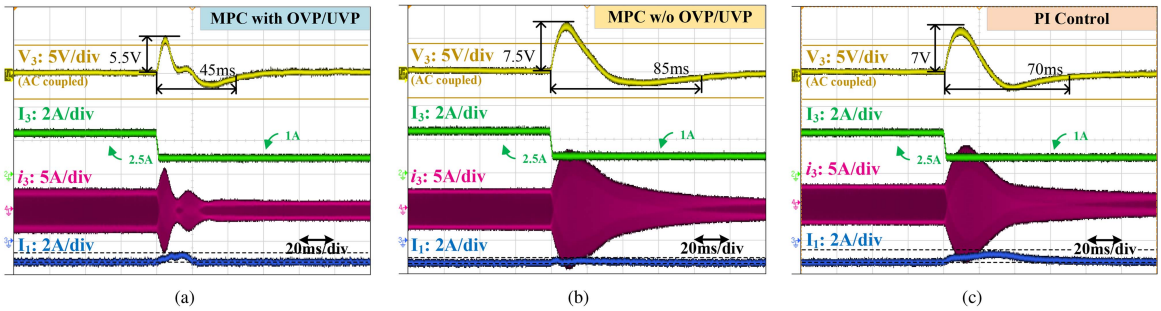

Fig. 13. Dynamic responses under a step load change at port #3 from 2.5 to 1 A. (a) MPC with OVP/UVP. (b) MPC without OVP/UVP. (c) PI control.

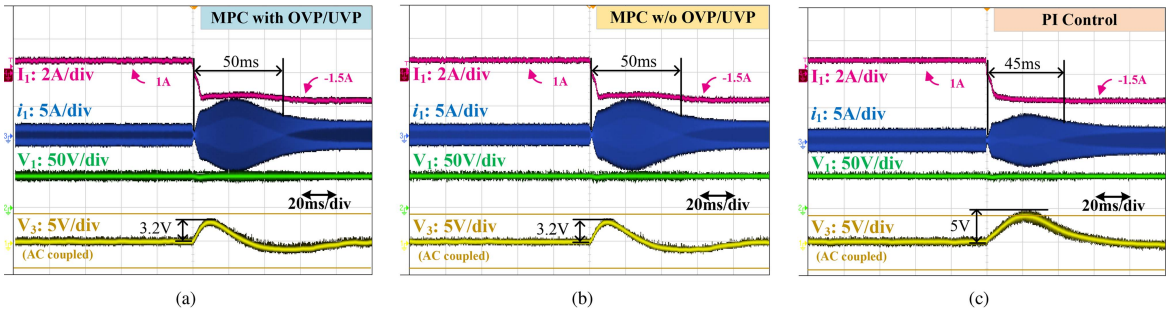

Fig. 14. Dynamic responses under a current reference change at port #1 from 1 to –1.5 A. (a) MPC with OVP/UVP. (b) MPC without OVP/UVP. (c) PI control.

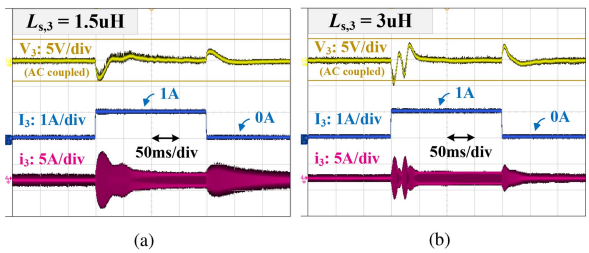

Fig. 15. Dynamic responses with parameter variations. (a) $L_{s,3} = 1.5\,\mu$H. (b) $L_{s,3} = 3\,\mu$H.

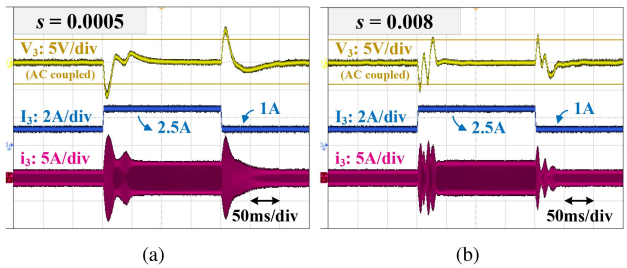

Fig. 16. Dynamic responses under different weighting factor s. (a) $s = 0.0005$. (b) $s = 0.008$.

Fig. 18, the parameters $T_s = 200\,\mu s$, $N_p = 3$ and $N_{iter} = 10$ are chosen accordingly to make sure that the total execution duration T_{mpc} can almost fill the sampling interval (i.e., T_s), while having relatively large N_p and N_{iter}. Note that due to the

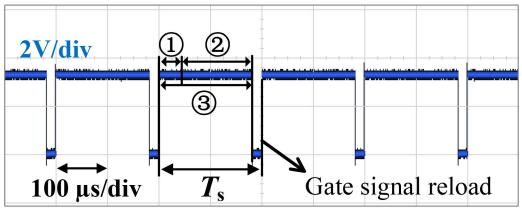

Fig. 17. Execution duration of the proposed CCS-MPC control within a single sampling interval [①: A/D conversion and parameters update (1 μs). ②: OSQP iteration (181 μs). ③: Total execution T_{mpc} (182 μs)].

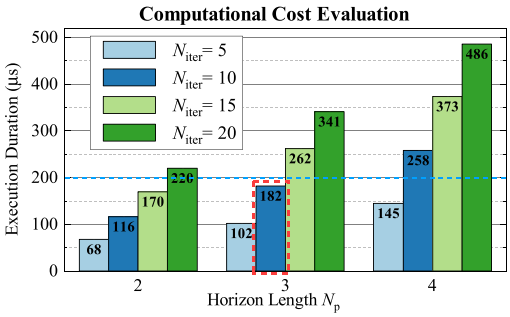

Fig. 18. Execution duration versus horizon length N_{p} and maximum number of iterations N_{iter}.

TABLE IV
KEY PARAMETERS AND SETTINGS OF OSQP SOLVER

Parameter	Description	Value/Setting
max_iter	Maximum number of iterations	$N_{\text{iter}} = 10$
check_termination	Check termination interval	$N_{\text{iter}} = 10$
warm_start	Perform warm starting	1

high computational burden, the control frequency is much lower than the switching frequency in this application. Therefore, another higher frequency timer (e.g., 100 kHz) can be enabled in the MCU for hard fault detection. Finally, thanks to future advances in QP solvers and MCU's computing performance, a possible faster control frequency can further accelerate the transient responses.

For reference purposes, the relevant key parameters and solver settings of OSQP are listed in Table IV below. Since the initial iteration point may affect the final solution, the so-called warm start strategy is adopted to improve the accuracy of the final solution, in which the solution of the previous time instant $k-1$ is set as the initial iteration point of the present time instant k.

VI. CONCLUSION

This article proposes and implements a constrained CCS-MPC-based energy routing control scheme for the MAB converters with OVP/UVP capability. The MPC control problem is first formulated as a QP problem by introducing soft constraints on the output voltage/current and hard constraints on the phase shift angle. Then, a new efficient QP solver OSQP with improved termination criteria is applied over a low-cost MCU, which is able to solve the QP problem online within a short sampling interval (i.e., 200 μs here) and thus achieve real-time implementation. Finally, the proposed control scheme is verified by simulation and experiments. The four-port 500 W prototyping energy router demonstrates effective OVP/UVP and guaranteed real-time performance.

APPENDIX

A. Parameters in "Δ-type" and "Y-type" equivalent circuit shown in Fig. 2(b) and (c)

$$L'_{\text{s,i}} = L_{\text{s,i}}(N_1/N_{\text{i}})^2, V'_{\text{i}} = V_{\text{i}}(N_1/N_{\text{i}})^2$$

$$L_{\text{ij}} = L'_{\text{s,i}}L'_{\text{s,j}}\sum_{k=1}^{n} 1/L'_{\text{s,k}}.$$

B. Small signal gains in predictive model (4)

$$G_{\text{ij}} = \begin{cases} \sum_{\text{j}\neq\text{i}}^{n} \frac{V_{\text{j}}}{2\pi f_{\text{sw}} L_{\text{ij}} N_{\text{j}} N_{\text{i}}} \left(1 - \frac{2|\Phi_{\text{i}} - \Phi_{\text{j}}|}{\pi}\right), & j = i \\ -\frac{V_{\text{j}}}{2\pi f_{\text{sw}} L_{\text{ij}} N_{\text{j}} N_{\text{i}}} \left(1 - \frac{2|\Phi_{\text{i}} - \Phi_{\text{j}}|}{\pi}\right), & j \neq i \end{cases}$$

$$H_{\text{ij}} = \frac{1}{2\pi f_{\text{sw}} L_{\text{ij}} N_{\text{j}} N_{\text{i}}} (\Phi_{\text{i}} - \Phi_{\text{j}}) \left(1 - \frac{|\Phi_{\text{i}} - \Phi_{\text{j}}|}{\pi}\right).$$

C. Matrix F and L in predictive law (6)

$$F = \left[\left(\sum_{i=1}^{1} CG^i\right)^{\text{T}} \quad \left(\sum_{i=1}^{2} CG^i\right)^{\text{T}} \quad \cdots \quad \left(\sum_{i=1}^{N_{\text{p}}} CG^i\right)^{\text{T}} \right]^{\text{T}}$$

$$L = \begin{bmatrix} \sum_{i=0}^{0} CG^i H & 0 & \cdots & 0 \\ \sum_{i=0}^{1} CG^i H & \sum_{i=0}^{0} CG^i H & \cdots & 0 \\ \vdots & \vdots & \ddots & \vdots \\ \sum_{i=0}^{N_{\text{p}}-1} CG^i H & \sum_{i=0}^{N_{\text{p}}-2} CG^i H & \cdots & \sum_{i=0}^{0} CG^i H \end{bmatrix}.$$

D. Weighting Factor Matrix Q, R in cost function (8)

$$Q = \text{diag}\{q_1, q_2, q_3\} = \text{diag}\left\{1/\tilde{I}_{L_1}^2, 1/\tilde{V}_{C_2}^2, 1/\tilde{V}_{C_3}^2\right\}$$

$$R = \text{diag}\{r_1, r_2, r_3\} = \text{diag}\{\lambda, \lambda, \lambda\}$$

where $\tilde{I}_{L_1}, \tilde{V}_{C_2}, \tilde{V}_{C_3}$ represent the rated value of $I_{L_1}, V_{C_2}, V_{C_3}$, respectively.

E. Matrix K, M, and c in soft constraints (12)

$$K = \begin{bmatrix} 1 & 0 & 0 \\ 1 & 0 & 0 \\ 1 & 0 & 0 \\ 0 & 1 & 0 \\ 0 & 1 & 0 \\ 0 & 1 & 0 \\ 0 & 0 & 1 \\ 0 & 0 & 1 \\ 0 & 0 & 1 \end{bmatrix} \quad M = \begin{bmatrix} 1 & 0 & 0 \\ -1 & 0 & 0 \\ 0 & 0 & 0 \\ 0 & 1 & 0 \\ 0 & -1 & 0 \\ 0 & 0 & 0 \\ 0 & 0 & 1 \\ 0 & 0 & -1 \\ 0 & 0 & 0 \end{bmatrix} \quad \boldsymbol{c} = \begin{bmatrix} -I_{\text{bat,max}} \\ I_{\text{bat,min}} \\ 0 \\ -V_{\text{PV,max}} \\ V_{\text{PV,min}} \\ 0 \\ -V_{\text{load,max}} \\ V_{\text{load,min}} \\ 0 \end{bmatrix}.$$

F. Matrix $\mathcal{Q}$, $\mathcal{R}$, $\mathcal{S}$, $\mathcal{K}$, $\mathcal{M}$, $\mathcal{N}$, and vector $\bar{\boldsymbol{c}}$ in QP problem

$$\mathcal{Q} = \text{blk diag}\{Q, Q, \ldots, Q\} \quad \mathcal{R} = \text{blk diag}\{R, R, \ldots, R\}$$

$$\mathcal{S} = \text{blk diag}\{S, S, \ldots, S\} \quad \mathcal{K} = \text{blk diag}\{K, K, \ldots, K\}$$

$$\mathcal{M} = \text{blk diag}\{M, M, \ldots, M\} \quad \bar{\boldsymbol{c}} = [\boldsymbol{c}, \boldsymbol{c}, \ldots, \boldsymbol{c}]$$

$$\mathcal{N} = \begin{bmatrix} \boldsymbol{I}_3 & \boldsymbol{0}_3 & \cdots & \boldsymbol{0}_3 \\ \boldsymbol{I}_3 & \boldsymbol{I}_3 & \cdots & \boldsymbol{0}_3 \\ \vdots & \vdots & \ddots & \boldsymbol{0}_3 \\ \boldsymbol{I}_3 & \boldsymbol{I}_3 & \cdots & \boldsymbol{I}_3 \end{bmatrix}.$$

REFERENCES

[1] P. Koohi, A. J. Watson, J. C. Clare, T. B. Soeiro, and P. W. Wheeler, "A survey on multi-active bridge dc-dc converters: Power flow decoupling techniques, applications, and challenges," *Energies*, vol. 16, no. 16, Aug. 2023, Art. no. 5927.

[2] S. Bandyopadhyay, P. Purgat, Z. Qin, and P. Bauer, "A multiactive bridge converter with inherently decoupled power flows," *IEEE Trans. Power Electron.*, vol. 36, no. 2, pp. 2231–2245, Feb. 2021.

[3] C. Liu et al., "An inductance-current-minimization optimization scheme based on hardware decoupling for modular multiactive-bridge converter," *IEEE Trans. Ind. Electron.*, vol. 71, no. 12, pp. 15793–15803, Dec. 2024.

[4] L. Gong et al., "Streamlined QPS control with magnetizing current injection for all-ZVS operation in decoupled-type triple active bridge converters," *IEEE Trans. Power Electron.*, vol. 39, no. 10, pp. 12894–12909, Oct. 2024.

[5] S. S. Chakraborty, S. Dey, and K. Hatua, "Design of a three-winding transformer for power decoupling of a three-port series resonant converter for an integrated on-board EV charger," *IEEE Trans. Power Electron.*, vol. 38, no. 11, pp. 14262–14273, Nov. 2023.

[6] Y. Cai, C. Gu, J. Li, J. Yang, G. Buticchi, and H. Zhang, "Dynamic performance enhancement of a triple active bridge with power decoupling-based configurable model predictive control," *IEEE Trans. Transport. Electrific.*, vol. 9, no. 2, pp. 3338–3349, Jun. 2023.

[7] L. Jiang, Y. Wu, L. Gong, Y. Li, J. Xu, and Y. Wang, "Comprehensive online decoupling strategy for LCTAB converters in EVs considering voltage fluctuation during load transient," *IEEE Trans. Power Electron.*, vol. 39, no. 11, pp. 14518–14532, Nov. 2024.

[8] S. Du, S. He, Q. Song, and J. Liu, "Power-flow decoupling method for the modular magnetic-coupled converter (MMCC)," *IEEE Trans. Ind. Electron.*, vol. 72, no. 6, pp. 5917–5924, Jun. 2025, doi: 10.1109/TIE.2024.3485623.

[9] A. A. Ibrahim, A. Zilio, T. Younis, D. Biadene, T. Caldognetto, and P. Mattavelli, "Optimal modulation of triple active bridge converters by an artificial-neural-network approach," *IEEE Trans. Ind. Electron.*, vol. 71, no. 3, pp. 2590–2600, Mar. 2024.

[10] M. Liao, H. Li, P. Wang, T. Sen, Y. Chen, and M. Chen, "Machine learning methods for feedforward power flow control of multi-active-bridge converters," *IEEE Trans. Power Electron.*, vol. 38, no. 2, pp. 1692–1707, Feb. 2023.

[11] H. Qin, C. Liu, Y. Shi, M. Liu, and C. Ma, "Prediction-based MIMO control of a multiport magnetic-coupled energy router," *IEEE Trans. Power Electron.*, vol. 39, no. 5, pp. 6409–6420, May 2024.

[12] N. Smith, "Understanding undervoltage lockout in power devices," 2018. [Online]. Available: https://www.ti.com/lit/an/slva769a/slva769a.pdf

[13] D. Kong, X. Gao, Z. Zhang, C. Liu, M. L. Heldwein, and R. Kennel, "Minimization of current stress for dual active bridge converters based on model predictive control with enhanced ZVS ability," *IEEE Trans. Ind. Electron.*, vol. 71, no. 8, pp. 8970–8980, Aug. 2024.

[14] D. Kong, Y. Wang, Z. Zhang, J. Rodriguez, R. Kennel, and M. L. Heldwein, "Transient DC offset mitigation for dual active bridge converters based on model predictive control with optimized dynamic performance," *IEEE Trans. Ind. Electron.*, vol. 72, no. 6, pp. 5906–5916, Jun. 2025.

[15] Z. Dong, Q. Chen, J. Qin, Z. Zhang, C. K. Tse, and Y. Xu, "Noise tolerance strategy based on virtual capacitor for DC-DC converters with continuous control set model predictive control," *IEEE Trans. Power Electron.*, vol. 39, no. 8, pp. 9084–9088, Aug. 2024.

[16] P. Karamanakos, E. Liegmann, T. Geyer, and R. Kennel, "Model predictive control of power electronic systems: Methods, results, and challenges," *IEEE Open J. Ind. Appl.*, vol. 1, pp. 95–114, 2020.

[17] S. Vazquez, J. Rodriguez, M. Rivera, L. G. Franquelo, and M. Norambuena, "Model predictive control for power converters and drives: Advances and trends," *IEEE Trans. Ind. Electron.*, vol. 64, no. 2, pp. 935–947, Feb. 2017.

[18] T. J. Besselmann, S. Van De Moortel, S. Almer, P. Jorg, and H. J. Ferreau, "Model predictive control in the multi-megawatt range," *IEEE Trans. Ind. Electron.*, vol. 63, no. 7, pp. 4641–4648, Jul. 2016.

[19] O. Wallscheid and E. F. B. Ngoumtsa, "Investigation of disturbance observers for model predictive current control in electric drives," *IEEE Trans. Power Electron.*, vol. 35, no. 12, pp. 13563–13572, Dec. 2020.

[20] A. Favato, P. G. Carlet, F. Toso, R. Torchio, and S. Bolognani, "Integral model predictive current control for synchronous motor drives," *IEEE Trans. Power Electron.*, vol. 36, no. 11, pp. 13293–13303, Nov. 2021.

[21] A. Zanelli, J. Kullick, H. M. Eldeeb, G. Frison, C. M. Hackl, and M. Diehl, "Continuous control set nonlinear model predictive control of reluctance synchronous machines," *IEEE Trans. Contr. Syst. Technol.*, vol. 30, no. 1, pp. 130–141, Jan. 2022.

[22] P. Acuna, C. A. Rojas, R. Baidya, R. P. Aguilera, and J. E. Fletcher, "On the impact of transients on multistep model predictive control for medium-voltage drives," *IEEE Trans. Power Electron.*, vol. 34, no. 9, pp. 8342–8355, Sep. 2019.

[23] D. Schmies, D. Weber, M. Schenke, J. Lange, and O. Wallscheid, "Optimal control of voltage forming grid inverters by model predictive control and reinforcement learning - Part I," *TechRxiv*, Jan. 2025, doi: 10.36227/techrxiv.173603468.84845950/v2.

[24] D. Weber, J. Lange, D. Schmies, M. Schenke, and O. Wallscheid, "Optimal control of voltage forming grid inverters by model predictive control and reinforcement learning - Part II," *TechRxiv*, Jan. 2025, 10.36227/techrxiv.173603469.93833780/v2.

[25] I. Hammoud et al., "On continuous-set model predictive control of permanent magnet synchronous machines," *IEEE Trans. Power Electron.*, vol. 37, no. 9, pp. 10360–10371, Sep. 2022.

[26] M. Rossi, P. Karamanakos, and F. Castelli-Dezza, "An indirect model predictive control method for grid-connected three-level neutral point clamped converters with LCL Filters," *IEEE Trans. Ind. Applicat.*, vol. 58, no. 3, pp. 3750–3768, May/Jun. 2022.

[27] S. Shao et al., "Modeling and advanced control of dual-active-bridge DC–DC converters: A review," *IEEE Trans. Power Electron.*, vol. 37, no. 2, pp. 1524–1547, Feb. 2022.

[28] X. Qu, H. Han, S.-C. Wong, C. K. Tse, and W. Chen, "Hybrid IPT topologies with constant current or constant voltage output for battery charging applications," *IEEE Trans. Power Electron.*, vol. 30, no. 11, pp. 6329–6337, Nov. 2015.

[29] J. Maciejowski, *Predictive Control: With Constraints*. Harlow, Poland: Prentice Hall, 2002.

[30] H. J. Ferreau, C. Kirches, A. Potschka, H. G. Bock, and M. Diehl, "qpOASES: A parametric active-set algorithm for quadratic programming," *Math. Prog. Comp.*, vol. 6, no. 4, pp. 327–363, Apr. 2014.

[31] B. Stellato, G. Banjac, P. Goulart, A. Bemporad, and S. Boyd, "OSQP: An operator splitting solver for quadratic programs," *Math. Prog. Comp.*, vol. 12, no. 4, pp. 637–672, Dec. 2020.

[32] G. Banjac, B. Stellato, N. Moehle, P. Goulart, A. Bemporad, and S. Boyd, "Embedded code generation using the OSQP solver," in *Proc. IEEE 56th Annu. Conf. Decis. Control*, Dec. 2017, pp. 1906–1911.

[33] P. Cortes et al., "Guidelines for weighting factors design in model predictive control of power converters and drives," in *Proc. IEEE Int. Conf. Ind. Technol.*, Feb. 2009, pp. 1–7.

[34] Z. Ullah Khan et al., "A review of degradation and reliability analysis of a solar PV module," *IEEE Access*, vol. 12, pp. 185036–185056, 2024.

[35] X. Pan, H. Li, Y. Liu, T. Zhao, C. Ju, and A. K. Rathore, "An overview and comprehensive comparative evaluation of current-fed-isolated-bidirectional DC/DC converter," *IEEE Trans. Power Electron.*, vol. 35, no. 3, pp. 2737–2763, Mar. 2020.

[36] M. Kheraluwala, R. Gascoigne, D. Divan, and E. Baumann, "Performance characterization of a high-power dual active bridge DC-to-DC converter," *IEEE Trans. Ind. Applicat.*, vol. 28, no. 6, pp. 1294–1301, Nov./Dec. 1992.

Haojun Qin (Student Member, IEEE) received the B.S. degree in automation from Wuhan University, Wuhan, China, in 2020, and the Ph.D. degree in electrical and computer engineering from the University of Michigan-Shanghai Jiao Tong University Joint Institute, Shanghai Jiao Tong University, Shanghai, China, in 2025.

His research interests include multiport power converters and applications of model predictive control.

Chang Liu (Student Member, IEEE) received the B.S. degree in electronic and computer engineering from Shanghai Jiao Tong University, Shanghai, China, in 2023. He is currently working toward the Ph.D. degree in electrical and computer engineering with the University of Michigan-Shanghai Jiao Tong University Joint Institute, Shanghai Jiao Tong University.

His research interests include high-frequency power electronics and bidirectional dc–dc converters.

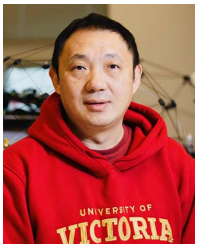

Yang Shi (Fellow, IEEE) received the B.Sc. and Ph.D. degrees in mechanical engineering and automatic control from Northwestern Polytechnical University, Xi'an, China, in 1994 and 1998, respectively, and the Ph.D. degree in electrical and computer engineering from the University of Alberta, Edmonton, AB, Canada, in 2005.

From 1998 to 2000, he was a Research Associate with the Department of Automation, Tsinghua University, Beijing, China. From 2005 to 2009, he was an Assistant Professor and Associate Professor with the Department of Mechanical Engineering, University of Saskatchewan, Saskatoon, SK, Canada. In 2009, he joined the University of Victoria, Victoria, BC, Canada, where he is currently a Professor with the Department of Mechanical Engineering. His research interests include networked and distributed systems, model predictive control, cyber–physical systems, robotics and mechatronics, navigation and control of autonomous systems, and energy system applications.

Dr. Shi was the recipient of the University of Saskatchewan Student Union Teaching Excellence Award in 2007, the Faculty of Engineering Teaching Excellence Award in 2012 at the University of Victoria (UVic), and the 2023 REACH Award for Excellence in Graduate Student Supervision and Mentorship. On research, he was the recipient of the JSPS Invitation Fellowship (short-term) in 2013, the UVic Craigdarroch Silver Medal for Excellence in Research in 2015, the Humboldt Research Fellowship for Experienced Researchers in 2018, CSME Mechatronics Medal (2023), IEEE Dr.-Ing. Eugene Mittelmann Achievement Award (2023), the 2024 IEEE Canada Outstanding Engineer Award. He was VP on Conference Activities of IEEE IES (2022–2025) and the Chair of IEEE IES Technical Committee on Industrial Cyber-Physical Systems. He is currently the IFAC Council Member and Editor-in-Chief for IEEE TRANSACTIONS ON INDUSTRIAL ELECTRONICS; he is also an Associate Editor for *Automatica*, IEEE TRANSACTIONS ON AUTOMATIC CONTROL, *Annual Review in Controls*, etc. He is a Fellow of ASME, CSME, Engineering Institute of Canada (EIC), Canadian Academy of Engineering (CAE), Royal Society of Canada (RSC), and a registered Professional Engineer in British Columbia, Canada.

Ming Liu (Senior Member, IEEE) received the B.S. degree in mechatronic engineering from Sichuan University, Sichuan, China, in 2007, and the Ph.D. degree in electrical and computer engineering from the University of Michigan-Shanghai Jiao Tong University Joint Institute, Shanghai Jiao Tong University, Shanghai, China, in 2017.

From 2017 to 2020, he was a Postdoctoral Research Fellow with the Department of Electrical Engineering, Princeton University, Princeton, NJ, USA. He joined the School of Electronic Information and Electrical Engineering, Shanghai Jiao Tong University, in 2020, where he is currently a Professor of Electrical Engineering. His research interests include megahertz wireless power transfer, plasma RF power amplifiers, and high frequency power electronics for emerging applications.

Dr. Liu was the recipient of the Top Ten Academic Star Award and the Excellent Ph.D. Thesis Award Nomination from the Shanghai Jiao Tong University, in 2016 and 2018, Research Excellence Award from AirFuel Alliance, USA, in 2019. He is the Vice Chair of the Wireless Power Transfer Systems (TC9), IEEE Power Electronics Society, and the Guest Editor and Associate Editor for the IEEE TRANSACTIONS ON INDUSTRIAL INFORMATICS, IEEE TRANSACTIONS ON POWER ELECTRONICS, and IEEE JOURNAL OF EMERGING AND SELECTED TOPICS IN POWER ELECTRONICS.

Chengbin Ma (Fellow, IEEE) received the B.S. degree in industrial automation from the East China University of Science and Technology, Shanghai, China, in 1997, and the M.S. and Ph.D. degrees in electrical engineering from The University of Tokyo, Tokyo, Japan, in 2001 and 2004, respectively.

From 2004 to 2006, he was an R&D Researcher with Servo Motor Laboratory, FANUC Limited, Yamanashi, Japan. From 2006 and 2008, he was a Postdoctoral Researcher with the Department of Mechanical and Aeronautical Engineering, University of California, Davis, CA, USA. In 2008, he joined the University of Michigan-Shanghai Jiao Tong University Joint Institute, Shanghai Jiao Tong University, Shanghai, China, where he is currently a Professor of electrical and computer engineering. His research interests include battery and energy management, wireless power transfer, dynamics and motion control, and a wide range of applications in electronic devices, electric vehicles, microgrids, and smart grids.

Dr. Ma was the recipient of many teaching and research awards at Shanghai Jiao Tong University, such as Koguan Top Ten Best Teacher Award in 2017 and Koguan Top Ten Research Group Award in 2014, and the recipient of Research Excellence Award from AirFuel Alliance, USA, in 2019, and Science and Technology Progress Award, China Power Supply Society, in 2024, etc. He is an IEEE Fellow and Associated Editor for IEEE TRANSACTIONS ON INDUSTRIAL INFORMATICS (2016–2022) and IEEE JOURNAL OF EMERGING AND SELECTED TOPICS IN INDUSTRIAL ELECTRONICS. He served as Delegate of Energy Cluster (2019–2020), and is currently Delegate of Cross-disciplinary Cluster (2024–2025), IEEE Industrial Electronics Society.